INTRINSIC KINETIC MODELING WITH EXPLICIT RADIATION ABSORPTION EFFECTS OF THE PHOTOCATALYTIC OXIDATION OF CYANIDE WITH TiO_2 AND SILICA-SUPPORTED TiO_2 SUSPENSIONS

Javier Marugán[a], Rafael van Grieken[a], Alberto E. Cassano[b], Orlando M. Alfano[b].

[a] Department of Chemical and Environmental Technology, ESCET, Universidad Rey Juan Carlos, C/ Tulipán s/n, 28933 Móstoles (Madrid), Spain,
Tel: +34 91 664 7007, Fax +34 91 488 7068, E-mail: javier.marugan@urjc.es

[b] Instituto de Desarrollo Tecnológico para la Industria Química (INTEC), (Universidad Nacional del Litoral-CONICET), CCT Santa Fe. Paraje El Pozo.
Colectora de la Ruta Nacional Nº 168, 3000 Santa Fe, Argentina
Tel: +54 342 451 1272/73, Fax +54 342 451 1087, E-mail: alfano@intec.unl.edu.ar

Published on
Applied Catalysis B: Environmental, 85: 48-60 (2008)
doi:10.1016/j.apcatb.2008.06.026

ABSTRACT

This study is focused on the kinetic modeling of the photocatalytic oxidation of cyanide in slurry reactors. The developed model is based on an accepted reaction mechanism and takes into account explicitly the differences in the local volumetric rate of photon absorption (LVRPA) produced by the unavoidable radiation profiles existing in the photoreactor. The model and its correspondent procedures for the evaluation of the LVRPA distribution and the estimation of the kinetic parameters have been successfully validated with both powder TiO_2 and TiO_2/SiO_2 photocatalysts with improved recovery properties. In both cases, the model reproduces the influence of the catalyst loading, the initial cyanide concentration, and the inlet radiation flux on the reaction rate, with errors below 5 %. The kinetic parameters estimated for the model are independent of the irradiation form, as well as the reactor size and its geometrical configuration, providing the necessary information for scaling-up and designing commercial scale photoreactors.

KEYWORDS: photocatalysis; kinetics; cyanide; titanium dioxide; supported photocatalyst.

1. INTRODUCTION

Cyanides constitute one of the most important families of pollutants present in the effluents of coal gasification [1,2] precious metal mining and electro-plating processes, in which the use of cyanide is almost essential [3,4]. The traditional technologies for cyanide oxidation, such as alkaline chlorination or the use of ozone or hydrogen peroxide, do not achieve the complete removal of metal-cyanide complexes [5]. In contrast, since the early work of Frank and Bard in 1977 [6], during the last decades, heterogeneous photocatalytic technologies have attracted increasing attention because they are potentially able to completely oxidize many organic compounds present in aqueous and gaseous effluents as it is demonstrated by the large number of scientific publications and reviews appeared in this field [7-13]. The problem described before, is not an exception, and many studies have demonstrated that photocatalytic oxidation processes show a high efficiency in the removal of free cyanides [2,6,14-17] and also refractory metal complexes [3,4,18,19]. Moreover, in the open literature there are reports of pilot plants developments for the photocatalytic treatment of cyanides in effluents derived from integrated gasification combined cycle (IGCC) power plants [20] and electroplating factories [21], including their economic assessment.

Heterogeneous photocatalytic technologies are based on the redox reactions induced by the electron-hole pairs formed in n-type semiconductors particles (usually TiO_2) upon illumination with radiation of energy greater than or equal to the band gap energy of the semiconductor. However, most of the research efforts have been devoted to the investigation of the fundamental mechanisms and phenomenological aspects of the process and only relatively few developments have succeeded in a complete description of the reaction kinetics due to lack of a rigorous evaluation of the absorbed radiation, i.e., most of the kinetic models reported in the literature do not properly consider the radiation profiles inside the photoreactor leading to equations that are only valid for the experimental setup in which the parameters have been estimated. Consequently, they become invalid for scaling-up and photoreactor design purposes.

In fact, most of the existing reports concentrate their efforts in describing the influence on the experimental reaction rate of variables such as catalyst loading, cyanide concentration, pH, presence of inorganic species, additional oxidants such as ozone or hydrogen peroxide, etc [6,14-17]. In some cases, kinetics studies have been performed,

usually concluding that the dependence of the reaction rate with the concentration of cyanide followed the Langmuir-Hinshelwood kinetic equation [15-17]. This simple equation, based on the application of the Langmuir adsorption isotherm to calculate the concentration of the reactant adsorbed on the solid, presents only two parameters: an adsorption equilibrium constant and a kinetic constant that includes the contribution to the reaction rate of variables such as catalyst concentration and radiation power. Despite the extended used of this kinetic model for the description of the photocatalytic reaction kinetics, several authors [22-24] have showed that the adsorption constant is not a pure equilibrium constant, as its value may depend, for example, on the radiation power. This fact could invalidate the theoretical assumptions of the model giving as a final result a pure empirical equation to correlate the experimental data. The most important challenge concerning the modeling of the photocatalytic reactions kinetics is the determination of the influence of the radiation power on the reaction rate. It is generally accepted that the photocatalytic reaction rate depends linearly with the incident light flux under low-radiation power conditions, but the exponent decreases to 0.5 under moderate to high-radiation power conditions, due to the relative increase of the influence of the second-order recombination rate [10,23,25,26].

In contrast with thermal reactors in which isothermal conditions can be easily achieved to determine the kinetic parameters, unavoidable radiation profiles are always present in photocatalytic reactors. Consequently, it is expected a progressive change in the dependence of the reaction rate with the radiation intensity from values close to 0.5 near the photoreactor irradiated surface to 1.0 in the darker regions. This means that a non-linear distribution of reaction rate values would be present, and that calculation of the radiation field inside the reactor is mandatory for a rigorous evaluation of the intrinsic kinetics of the process [27-33]. Consequently, whereas the use of equations that correlate the macroscopic reaction rate with the incident photon flux are only valid for the experimental setup in which they have been developed, the determination of the intrinsic kinetics is absolutely required for simulating different reactor configurations and irradiation conditions with engineering prospects.

Concerning the arrangement of the catalyst inside the reactor, to maximize the activity, photocatalysts usually require semiconductor suspensions with particle sizes in the nanometer range [34]. This choice, hinders the commercial applications of aqueous TiO_2-based produced by the need for recovery the catalyst after the reaction has been completed.

Moreover, recent studies have raised concerns about the potential toxicity of titanium dioxide nanoparticles, not only for mammals [35] but also for human cells [36]. For these reasons, many attempts have been made to develop supported photocatalysts [37], either in the form of fixed beds [38], fluidized beds [39,40] or slurries [41,42]. Among them, silica-supported TiO_2 particulate materials appear to be a promising way to improve the recovery properties of the catalyst while maintaining an acceptable level of photoactivity [43].

This study is focused on the development of an intrinsic kinetic model with explicit radiation absorption effects applied to the photocatalytic oxidation of cyanide in slurry reactors. The validation of the model has been carried out using suspensions of commercial TiO_2 and TiO_2/SiO_2 photocatalysts of larger size and, consequently, with improved recovery properties. The kinetic parameters estimated for the model should be independent of the irradiation form, as well as the reactor size and its geometrical configuration, providing the necessary information for scaling-up and design of commercial-scale photoreactors.

2. EXPERIMENTAL

2.1. Catalysts

Two different photocatalysts have been tested and compared: i) A pure TiO_2 material (Aldrich, >99% anatase, 7.1 $m^2 g^{-1}$ of specific surface area); and ii) a TiO_2/SiO_2 mixed material with a nominal content of 40 wt% of TiO_2 synthesized by incorporating titania into a silica support (INEOS Silica ES70Y, 257 $m^2 g^{-1}$ of specific surface area) through a sol-gel method which leads to titanium dioxide nanocrystals homogeneously distributed over the silica porous network with an average size of 7.2 nm. The fraction of the total specific surface area of the 40%TiO_2/SiO_2 material corresponding to titania has been estimated in 19.3 $m^2 g^{-1}$ using a novel procedure recently developed [44]. A detailed physicochemical characterization and quantitative values of the optical properties of both catalysts suspensions can be found elsewhere [45].

2.2. Photoreactor

The experimental setup for the photocatalytic reactions, represented in Figure 1, consists of a cylindrical reactor 6 cm long and 5 cm in diameter, operating in a closed recirculating circuit driven by a centrifugal pump and with a stirred reservoir tank of 2 L volume equipped with a device for withdrawal of samples. The liquid flow was set above 100 $cm^3\ s^{-1}$ to ensure good mixing conditions in the photoreactor and a differential conversion per pass. The photoreactor is made of borosilicate glass and presents a circular flat window externally treated with HF to produce a ground glass texture. The radiation enters the reactor through this window, which allows the assumption of a diffuse incoming radiation in the boundary condition of the radiation transport equation.

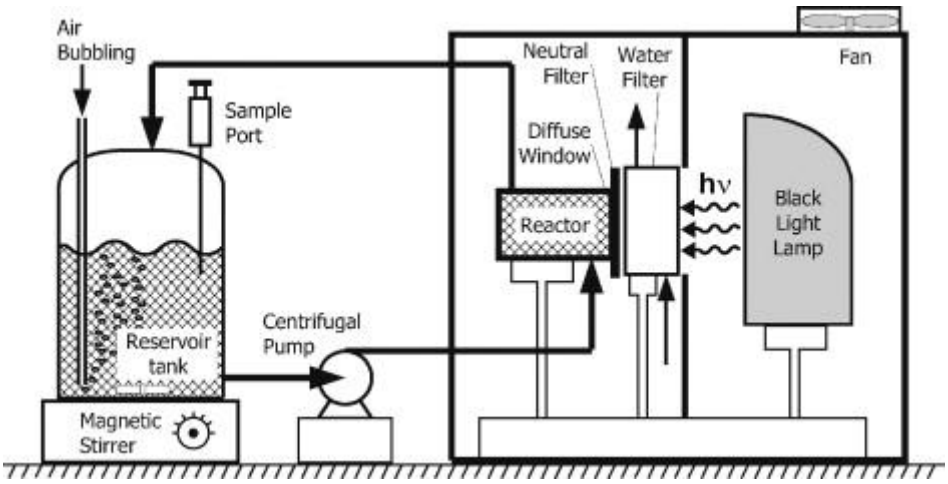

Figure 1. Schematic representation of the experimental photoreactor setup (see text for details).

Illumination was carried out using an Osram Ultramed 400W black light lamp that provides 82 W of nominal UV-A radiation power. Radiation enters the photoreactor after crossing a water filter to remove infrared radiation and to avoid overheating of the suspension, and a neutral filter that controls the radiation flux entering the reactor. Neutral filters consist of a polymeric substrate in which a controlled black coverage level is achieved by high-quality laser printing using CorelDraw® software. The reproducibility and stability of the filters after several hours of irradiation has been positively verified by checking the intensity and spectrum of the filtered UV radiation with a Gigahertz-Optik X97 irradiance meter and a Varian Cary 500 Scan UV-Vis-NIR spectrophotometer, respectively. Detailed characteristics of the filters, emission spectrum of the lamp and quantitative values of the radiation fluxes determined by ferrioxalate actinometry can be found elsewhere [46].

Between the lamp and the neutral density filter, a shutter was interposed that was only removed after the whole system (reactor flow rate as well as lamp and tank temperatures) have reached the steady-state operation. Both the reactor and the lamp chambers are placed inside a black box to avoid uncontrolled radiation entering the photoreactor. The reservoir tank and pipes are also masked to avoid reactions outside the photoreactor.

2.3. Reaction Procedure

Experiments of cyanide photooxidation were carried out at 25 ± 2ºC. Deionized water (Milli-Q®, 18.2 MΩ cm) was used to prepare the solutions of potassium cyanide (Panreac, reagent grade) and the pH was adjusted to 12 with sodium hydroxide (Scharlab, reagent grade). After the addition of the catalyst, the suspension was stirred and saturated with molecular oxygen by bubbling the gas for 30 minutes. In the meantime, the lamp was switched on to stabilize its emission power and spectrum.

During the reaction, samples were taken every 10 min from the reservoir tank and filtered through 0.22 μm nylon membranes to remove the catalyst before analysis. Temperature and pH measurements were performed to check that both parameters remained essentially constant. Cyanide analysis was carried out using the pyridine-barbituric standard colorimetric method [47], averaging four independent measurements to increase the statistical significance of the analytical results obtained when operating with low cyanide conversion.

3. RESULTS

Three different series of experiments were carried out to check the influence of the main parameters governing the cyanide photooxidation kinetics with each catalytic material:

i) The incident radiation flux (q^0) was varied in the range $0.255 \times 10^{-6} – 2.89 \times 10^{-6}$ Einstein cm^{-2} s^{-1} using neutral filters as described in the experimental section.

ii) Initial cyanide concentration (C^0_{CN}-) was studied in the range $0.185 \times 10^{-6} – 3.85 \times 10^{-6}$ mol cm^{-3}.

iii) The values of the catalyst concentration (C_{cat}) were different for every material in order to obtain comparable values of the volumetric rate of photon absorption [48]. Powder TiO_2 concentration was varied in the range $0.32 \times 10^{-4} - 5.0 \times 10^{-4}$ g cm^{-3} whereas TiO_2/SiO_2 was studied in the range $0.32 \times 10^{-3} - 5.0 \times 10^{-3}$ g cm^{-3}.

All these values have been selected from previous results reported in the literature [16,17,48] in order to cover the experimental region in which the reaction rate of cyanide photooxidation is clearly influenced by the studied variables.

To analyze the results, initial reaction rates were calculated because in all cases conversions are small enough to consider that: i) the amount of formed products is negligible and ii) the stoichiometric consumption of oxygen is low and consequently, the dissolved oxygen could be considered constant, and iii) the change in cyanide concentration is low and it could be assumed that does not affect the reaction rate. Initial reaction rates values have been calculated from the slope of the straight line fitting of the cyanide concentration profiles determined by averaging four replicates of the cyanide analysis in order to reduce the impact of the analytical error derived from the low level of cyanide conversion. More details of this procedure can be found elsewhere [48].

Table 1 summarizes the results obtained for the experimental reaction rate of cyanide photooxidation averaged over the reactor volume. These values have been calculated from the cyanide concentration profiles in the reservoir tank assuming that: i) the system is perfectly mixed; ii) there are no mass transport limitations; iii) the conversion per pass in the reactor is differential; and iv) there are no parallel dark reactions. Under these assumptions the mass cyanide balance can be expressed as follows:

$$\varepsilon_L \left. \frac{\mathrm{d}C_{CN^-}\ t}{\mathrm{d}t} \right|_{Tk} = -\frac{V_R}{V_T} \left\langle r_{CN^-}(\underline{x},t) \right\rangle_{V_R} \qquad (1)$$

where ε_L is the liquid hold-up ($\varepsilon_L \approx 1$); C_{CN^-} is the molar concentration of cyanide; t denotes reaction time; *Tk*, *R* and *T* subscripts refer to the tank, reactor and total, respectively; and $\left\langle r_{CN^-}\ x,t\ \right\rangle_{V_R}$ is the cyanide oxidation rate averaged over the reactor volume. The values

reported in Table 1 have been calculated from the plot of the cyanide concentration in the tank vs. time according to the expression:

$$\left\langle r^{0}_{CN^-} \right\rangle^{Exp}_{V_R} = -\frac{V_T}{V_R} \lim_{t \to 0} \left. \frac{\mathrm{d}C_{CN^-}\ t}{\mathrm{d}t} \right|_{Tk} \qquad (2)$$

Table 1. Experimental values of the initial reaction rate of cyanide photooxidation.

			TiO_2		TiO_2/SiO_2	
Exp.	$q^0 \times 10^6$ (E cm^{-2} s^{-1})	$C^0_{CN^-} \times 10^6$ (mol cm^{-3})	$C_{cat} \times 10^4$ (g cm^{-3})	$\left\langle r^{0}_{CN^-} \right\rangle^{Exp}_{V_R} \times 10^{10}$ (mol cm^{-3} s^{-1})	$C_{cat} \times 10^3$ (g cm^{-3})	$\left\langle r^{0}_{CN^-} \right\rangle^{Exp}_{V_R} \times 10^{10}$ (mol cm^{-3} s^{-1})
1	1.30	1.15	0.32	2.51	0.32	1.01
2	1.30	1.15	1.00	4.71	1.00	2.13
3	1.30	1.15	2.00	5.53 ± 0.52	2.00	3.04 ± 0.43
4	1.30	1.15	3.00	5.95	3.00	3.82
5	1.30	1.15	3.68	5.89	3.68	4.45
6	1.30	1.15	5.00	5.82	5.00	4.85
7	1.30	0.185	2.00	1.79	2.00	1.06
8	1.30	0.577	2.00	2.80	2.00	1.98
9	1.30	1.73	2.00	8.28	2.00	3.79
10	1.30	2.12	2.00	10.9	2.00	4.60
12	1.30	3.08	2.00	15.8	2.00	5.49
12	1.30	3.85	2.00	17.1	2.00	5.83
13	0.255	1.15	2.00	1.80	2.00	1.16
14	0.586	1.15	2.00	3.08	2.00	2.02
15	2.00	1.15	2.00	7.18	2.00	4.02
16	2.33	1.15	2.00	7.80	2.00	4.68
17	2.89	1.15	2.00	9.03	2.00	5.44

The experimental error has been estimated by the standard deviation of three different replicates of Exp. 3.

Table 1 shows that the initial reaction rate of the photocatalytic oxidation of cyanide clearly increases for higher catalyst concentration, initial cyanide concentration and inlet radiation fluxes, as was obviously expected. Considering the explored experimental variables, only the case of radiation absorption saturation at high catalyst loadings could have been observed.

4. DISCUSSION

4.1. Kinetic Model

The proposed kinetic model for the photocatalytic degradation of cyanide in aqueous suspension is based on the reaction sequence reported by [17]. The main reaction steps which contribute to the photocatalytic degradation of cyanide on the surface of TiO_2 under UV radiation are illustrated in Table 2.

Table 2. Reaction scheme for cyanide photocatalytic degradation.

Reaction Step			Step Number
$TiO_2 + h\nu$	$\rightarrow$	$TiO_2 + e^- + h^+$	1
$e^- + h^+$	$\rightarrow$	heat	2
$e^- + O_2$	$\rightarrow$	$\bullet O_2^-$	3
$\bullet O_2^- + H_2O$	$\rightarrow$	$HO_2\bullet + HO^-$	4
$HO_2\bullet + e^-$	$\rightarrow$	HO_2^-	5
$\equiv TiO^- + h^+$	$\rightarrow$	$\equiv TiO\bullet$	6
$HO^- + h^+$	$\rightarrow$	$HO\bullet$	7
$HO^- + \equiv TiO\bullet$	$\rightarrow$	$HO\bullet + \equiv TiO^-$	8
$CN^- + h^+$	$\rightarrow$	$CN\bullet$	9
$CN^- + \equiv TiO\bullet$	$\rightarrow$	$CN\bullet + \equiv TiO^-$	10
$\equiv TiO\bullet + e^-$	$\rightarrow$	$\equiv TiO^-$	11
$2\ CN\bullet$	$\rightarrow$	$(CN)_2$	12
$(CN)_2 + 2\ HO^-$	$\rightarrow$	$CNO^- + CN^- + H_2O$	13
$2\ HO\bullet$	$\rightarrow$	H_2O_2	14
$2\ H_2O_2$	$\rightarrow$	$2\ H_2O + O_2$	15

The cyanide degradation rate expression is derived from the following assumptions (see Appendix): (i) photocatalytic reaction takes place on the catalyst surface among adsorbed species, (ii) the steady state approximation may be applied for unstable reaction intermediates such as radicals and semiconductor electrons and holes [49], (iii) the concentration of electrons and holes are approximately equal ($[e^-] \approx [h^+]$) [49], (iv) the rate of electron-hole generation is equal to the product of LVRPA (e^a) and the average value of the primary quantum yield over the working wavelength interval ($\overline{\varphi}$) [27], (v) cyanide is oxidized by the surface trapped holes ($\equiv TiO\bullet$) [17], (vi), the concentrations of water and hydroxyl ions on the TiO_2 surface are almost constant, (vii) equilibrium conditions are achieved between the adsorbed and bulk concentrations of the organic compounds, (viii) a competitive adsorption mechanism for cyanide and its main intermediates is assumed, (ix) the oxygen concentration

is constant, and (x) the adsorption of oxygen on the catalyst surface sites does not compete with the organic compounds [49].

As indicated in Appendix A, the following kinetic expression can be derived:

$$r_{CN^-} = -S_g C_{cat} \frac{\alpha_1 [\mathrm{CN}_b^-]}{1+\alpha_3 [\mathrm{CN}_b^-] + \sum_P K_P [\mathrm{P}_b]} \left[-1 + \sqrt{1 + \frac{\alpha_2}{S_g C_{cat}} e^a} \right] \quad (3)$$

where r_{CN}- is the cyanide photocatalytic degradation rate per unit suspension volume, C_{CN}- the cyanide molar concentration in the suspension bulk, e^a the LVRPA, S_g the catalyst specific surface area, C_{cat} the catalyst mass concentration, and α_1, α_2, and α_3 are kinetic parameters.

Notice that the proposed kinetic model provides a more general rate expression compared to that previously reported by Chiang et al. [17]. For example, Equation (3) gives an explicit dependence of the photon absorption effects on the cyanide degradation rate. This kinetic model reproduces the two limiting cases normally reported in the literature on photocatalytic degradation of contaminants in aqueous solution [27,49]: (i) when the incident radiation flux on the reactor window is moderated or high, a typical square root dependence with respect to the LVRPA is obtained, and (ii) when the incident photon flux is low, with a Taylor series expansion of the square root term [27], it can be shown that a linear dependence with the LVRPA is observed. It is also worth noting that the photon absorption rate is generally a strong function of position inside the photocatalytic reactor due to the high radiation absorption generated by these TiO_2 suspensions. Accordingly, both kinetic regimes may coexist inside the same photoreactor and the general reaction rate expression must be used to describe the reactor behavior. Besides, Equation (3) can be used to assess the effects of the specific surface area and of the catalyst mass concentration on the cyanide photocatalytic degradation rate.

Assuming negligible concentration of intermediate products (initial reaction rate calculations), the estimation of the reaction rate of the photocatalytic oxidation of cyanide just requires the values of the catalysts concentration, cyanide concentration and photon absorption rate in the reactor volume. However, whereas the catalyst and cyanide

concentrations can be assumed uniform in the whole reactor volume under well-mixed and differential conversion conditions, the unavoidable radiation profiles along the reactor leads to a highly inhomogeneous distribution of e^a inside the reactor, with maximum values near the irradiated window and almost negligible values on the opposite darker part of the reactor.

Accordingly, the mass balance for C_{CN^-} [Eq. (1)] must be used to average the rate over the reactor volume according to the expression:

$$\left\langle r^0_{CN^-} \right\rangle^{KM}_{V_R} = -S_g C_{cat} \frac{\alpha_1 C_{CN^-}}{1+\alpha_3 C_{CN^-}} \left(-1 + \left\langle \sqrt{1+\frac{\alpha_2 e^a}{S_g C_{cat}}} \right\rangle_{V_R} \right) \tag{4}$$

Equation (4) indicates that the evaluation of the reaction rate requires the knowledge of the LVRPA (e^a_λ) that will have to be integrated over the whole useful range of wavelengths.

4.2. Evaluation of the LVRPA

The radiation field inside the photoreactor can be calculated by solving the Radiative Transfer Equation (RTE) that describes the transport of photons [50]. Assuming that the emission of radiation could be considered negligible at the low working temperatures of the photocatalytic processes, and that steady state condition could be applied, *e.g.* the optical properties of the suspension do not change with time, the RTE takes the following expression:

$$\frac{\mathrm{d}I_{\lambda,\underline{\Omega}}(\underline{x})}{\mathrm{d}s} = -\underbrace{\kappa_\lambda(\underline{x})I_{\lambda,\underline{\Omega}}(\underline{x})}_{\text{ABSORPTION}} - \underbrace{\sigma_\lambda(\underline{x})I_{\lambda,\underline{\Omega}}(\underline{x})}_{\text{OUT-SCATTERING}} + \underbrace{\frac{\sigma_\lambda(\underline{x})}{4\pi}\int_{\Omega'=4\pi} p(\underline{\Omega}' \rightarrow \underline{\Omega})I_{\lambda,\underline{\Omega}'}(\underline{x})\mathrm{d}\Omega'}_{\text{IN-SCATTERING SOURCE TERM}} \tag{5}$$

This integro-differential equation described the monochromatic transport of spectral specific intensities, along the directional spatial variable (*s*) and its solution provides the value of the intensity of photons for each differential elementary volume of the reactor and for each direction of radiation propagation in the spherical space (θ,ϕ) and the wavelength

λ, $I_{\lambda,\underline{\Omega}}(\underline{x})$. This equation must be solved for every single wavelength (λ) of the discretized wavelength range in which the overlapping between the emission spectrum of the lamp and the absorption coefficient of the catalysts is produced. Consequently, the spectral distribution of the optical properties of the catalyst suspension is required. These optical properties are: (i) the volumetric absorption coefficient, κ_λ, (ii) the volumetric scattering coefficient, σ_λ, and (iii) the scattering phase function, $p_\lambda(\underline{\Omega}' \rightarrow \underline{\Omega})$ that very often may be assumed independent of (λ). The latter function describes the angular distribution of the scattered radiation. In previous reports we have shown that the Henyey-Greentein's phase function could be successfully used to describe the scattering of both TiO_2 [51] and TiO_2/SiO_2 [45] photocatalyst suspensions. This function is expressed as follows:

$$p(\underline{\Omega}\cdot\underline{\Omega}') = p(\cos\alpha) = \frac{1-g^2}{1+g^2-2g\cos\alpha^{3/2}} \qquad (6)$$

Equation (6) presents the advantage of being able to reproduce very different scattering radiation distributions with only one adjustable parameter, the asymmetry factor *g*. The values of κ, σ and *g* used in this work correspond with those previously reported [45,51].

The rigorous numerical solution of the radiation propagation in multidimensional systems could be achieved by two main groups of procedures: (i) probabilistic models, especially Monte Carlo simulations [50,52-55] and (ii) discretization methods for the integration of the Radiative Transfer Equation (RTE), from which the Discrete Ordinate Method (DOM) has shown a wide range of applications with no restrictions about the geometry or the scattering anisotropy of the system [56-60].

Considering that the aqueous solution of cyanide does not absorb radiation in the near UV region, the radiation field inside the reactor can be assumed independent of the cyanide concentration, but it strongly depends on the catalyst concentration and the inlet radiation flux. The values of the monochromatic inlet radiation fluxes q_λ^0 have been estimated from the total incoming radiation fluxes measured by ferrioxalate actinometry. With this purpose, the relative values of the radiation emission power produced by the lamp at each wavelength of the employed discretized interval must be used. The result provides the boundary condition

for the solution of the RTE employing the DOM. This method consists in the transformation of the integro-differential RTE into a system of algebraic equations that describe the transport of photons in such way that they can be solved following the direction of propagation, starting from the values provided by the boundary condition.

The numerical procedure for the evaluation of the radiation field inside the photoreactor through the resolution of the RTE using the DOM is detailed in Appendix B. Once the radiation intensities are known, the local volumetric rate of photon absorption (LVRPA) in each point of the photoreactor, e^a, can be calculated by integrating, over the studied wavelength range, the product of the monochromatic absorption coefficient multiplied by the total incident monochromatic radiation, that corresponds to the integration of the monochromatic intensities over the whole spherical space of directions:

$$e^a = \int_{\lambda_1}^{\lambda_2} \kappa_\lambda(\underline{x}) \cdot \int_{\Omega = 4\pi} I_{\lambda,\underline{\Omega}}(\underline{x})\, \mathrm{d}\Omega\, \mathrm{d}\lambda \tag{7}$$

4.3. Estimation of the Kinetic Parameters

The estimation of the kinetic parameters for Equation (4) has been carried out following the conceptual flowchart displayed in Figure 2. Starting from the experimental conditions in which the reactions have been carried out, the polychromatic radiation flux entering the reactor is obtained from actinometric results and the known lamp emission spectrum. This is the boundary condition required for the evaluation of the radiation field in the photoreactor through the resolution of the RTE using the optical properties of the suspension. Once the distribution of radiation intensity inside the reactor is known, the values of the LVRPA in every differential volume of the reactor are calculated. These values are required for the kinetic model equation that leads to the distribution of reaction rate values in the photoreactor. Finally, the reaction rates averaged in the whole reactor volume are compared with their correspondent experimental values to estimate the kinetic parameters α_1, α_2, and α_3 using a Marquardt-Levenberg non-linear regression algorithm.

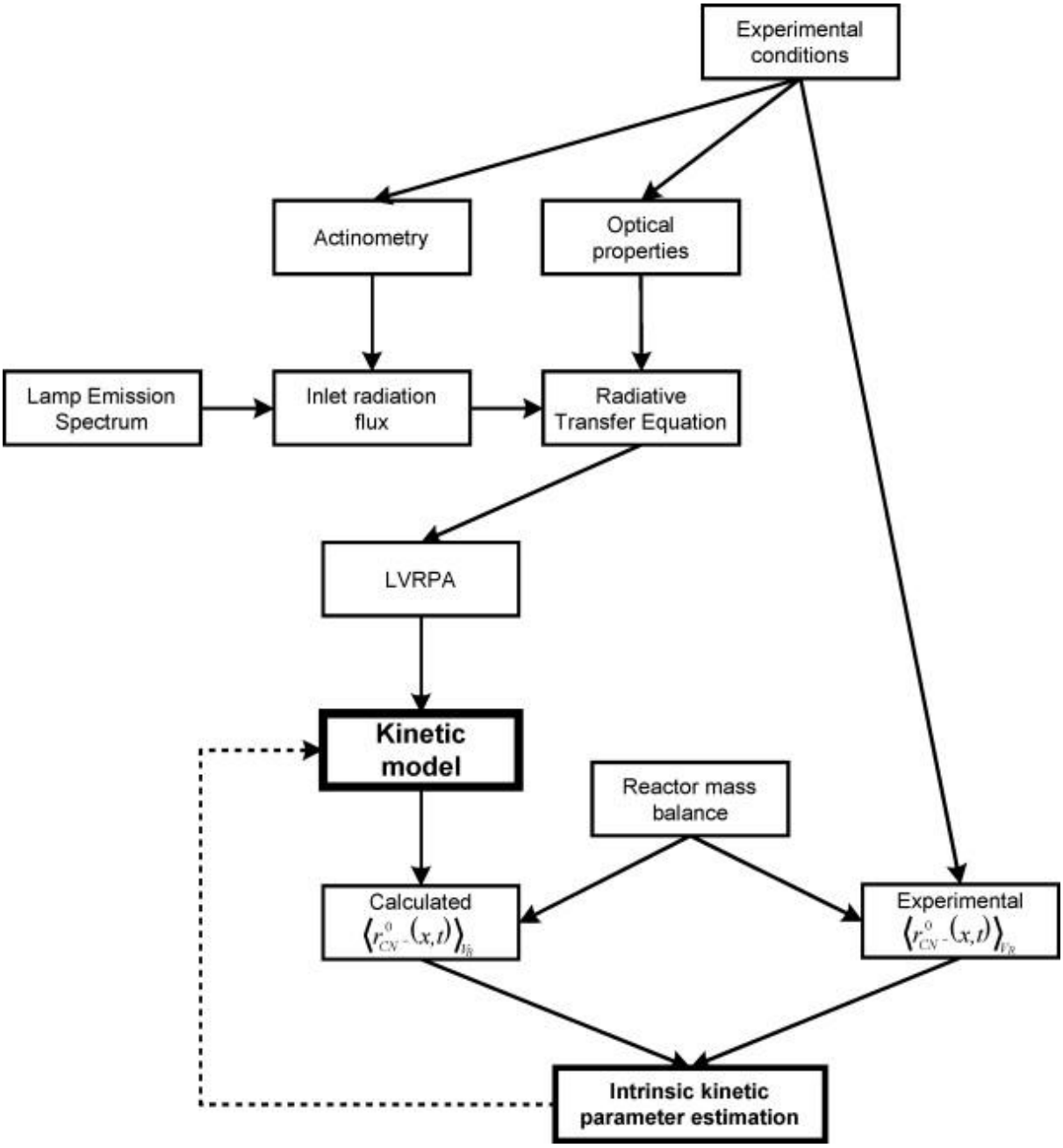

Figure 2. Conceptual flowchart of the procedure for estimating the intrinsic kinetic parameters.

The kinetic model equations thus obtained are:

$$\left\langle r^{0}_{CN^-} \right\rangle^{KM}_{V_R} = -S_g C_{cat} \frac{7.95 \pm 0.13 \times 10^{-6} \times C_{CN^-}}{1 + 1.91 \pm 0.65 \times 10^{4} \times C_{CN^-}} \left(-1 + \left\langle \sqrt{1 + \frac{1.16 \pm 0.04 \times 10^{11} \times e^{a}}{S_g C_{cat}}} \right\rangle_{V_R} \right) \quad (8)$$

Correlation coefficient = 0.9983

NRMSE = 3.5%

F = 3018

for TiO_2 ($S_g = 7.1 \times 10^4$ $cm^2 \cdot g^{-1}$) and

$$\left\langle r^{0}_{CN^-} \right\rangle^{KM}_{V_R} = -S_g C_{cat} \frac{9.94 \pm 0.14 \times 10^{-7} \times C_{CN^-}}{1 + 5.27 \pm 0.16 \times 10^{5} \times C_{CN^-}} \left(-1 + \left\langle \sqrt{1 + \frac{1.99 \pm 0.05 \times 10^{11} \times e^{a}}{S_g C_{cat}}} \right\rangle_{V_R} \right) \quad (9)$$

Correlation coefficient = 0.9974

NRMSE = 4.8%

F = 2051

for TiO_2/SiO_2 ($S_g = 19.3 \times 10^4$ $cm^2 \cdot g^{-1}$). It is important to remark that the value of S_g of the material 40%TiO_2/SiO_2 corresponds only to the active semiconductor surface, that is the titania, as the surface area of the silica support is completely inactive. The fraction of the total surface area of the mixed oxide corresponding to TiO_2 has been estimated using a novel method recently developed [44].

As it can be seen, in both cases good correlation coefficients and normalized root mean square errors are obtained. Moreover, the 95% confidence intervals of the kinetic parameters are quite acceptable. Depending on the significance of the parameter α_3, two-parameter model fittings (without α_3) could be tested, leading to the following results:

$$\left\langle r^{0}_{CN^-} \right\rangle^{KM}_{V_R} = -S_g C_{cat} \times 6.34 \pm 0.11 \times 10^{-6} \times C_{CN^-} \left(-1 + \left\langle \sqrt{1 + \frac{1.64 \pm 0.05 \times 10^{11} \times e^{a}}{S_g C_{cat}}} \right\rangle_{V_R} \right) \quad (10)$$

Correlation coefficient = 0.9982

NRMSE = 3.7%

F = 4853

for TiO_2, and

$$\left\langle r^{0}_{CN^-} \right\rangle^{KM}_{V_R} = -S_g C_{cat} \times \ 7.72 \pm 0.50 \ \times 10^{-7} \times C_{CN^-} \left(-1 + \left\langle \sqrt{1 + \frac{9.70 \pm 0.89 \ \times 10^{10} \times e^{a}}{S_g C_{cat}}} \right\rangle_{V_R} \right) \quad (11)$$

Correlation coefficient = 0.9844

NRMSE = 20.6%

F = 536

for TiO_2/SiO_2. In the case of TiO_2, the removal of α_3 only produces a small increase in the error of the estimated parameters, whereas the plausibility of the model given by the F-test is substantially increased. On the contrary, the use of the two-parameter model leads to a significant increase in the fitting error in the case of TiO_2/SiO_2, together with a decrease in the F-value.

Figure 3 show the agreement of the experimental results of the photocatalytic oxidation of cyanide with TiO_2 achieved with the developed kinetic model. Only the fitting with the two-parameter model represented by Eq. (10) is displayed, since no differences can be observed when it is compared to the three-parameter model [Eq. (8)]. It can be seen the influence of the three studied operating variables are successfully reproduced. Similarly, Figure 4 displays the correspondence of the experimental results obtained with TiO_2/SiO_2 with both the two- and the three-parameter models. In this case, important differences are observed between both models with significant deviations at the highest values of catalyst concentration, cyanide concentration and inlet radiation fluxes.

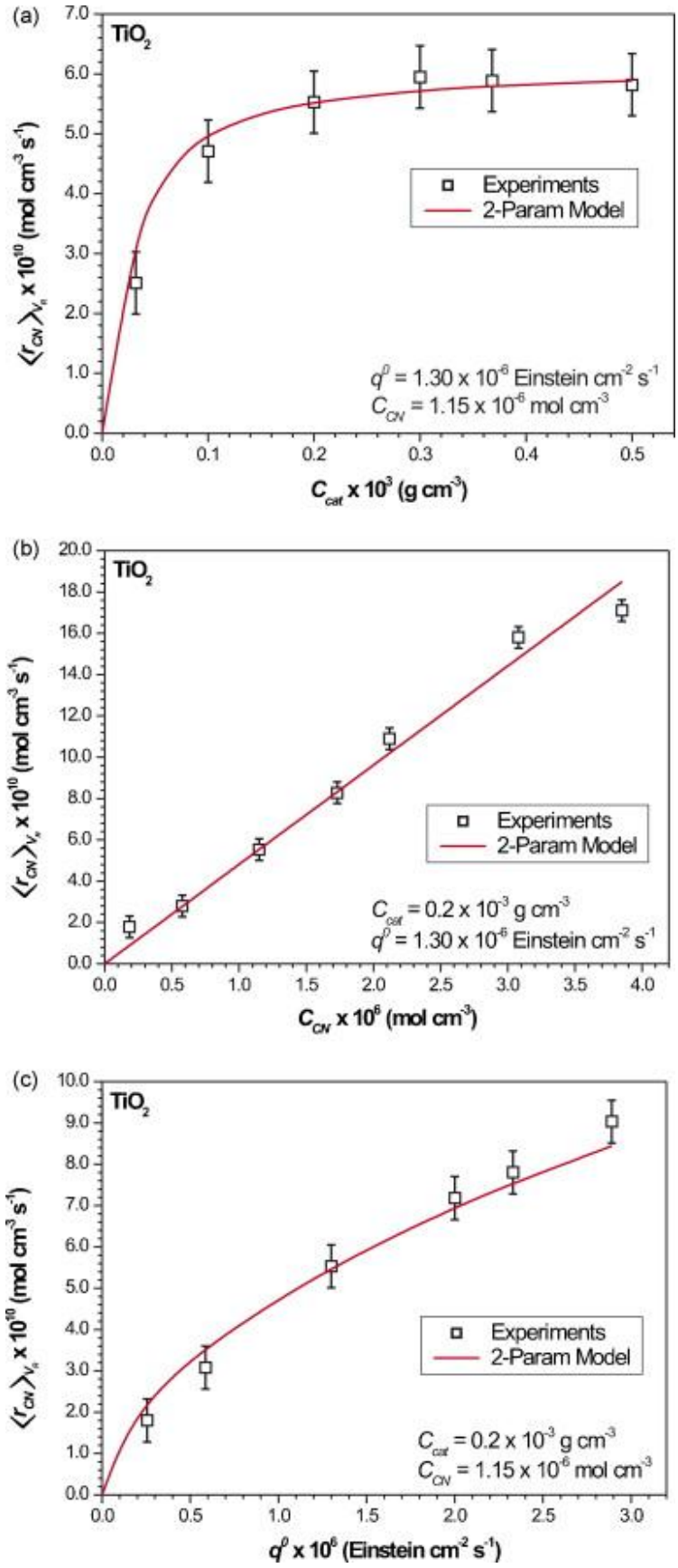

Figure 3. Experimental results of the initial reaction rate for the cyanide photocatalytic oxidation with powder TiO_2 and two-parameter model using Eq. 10.

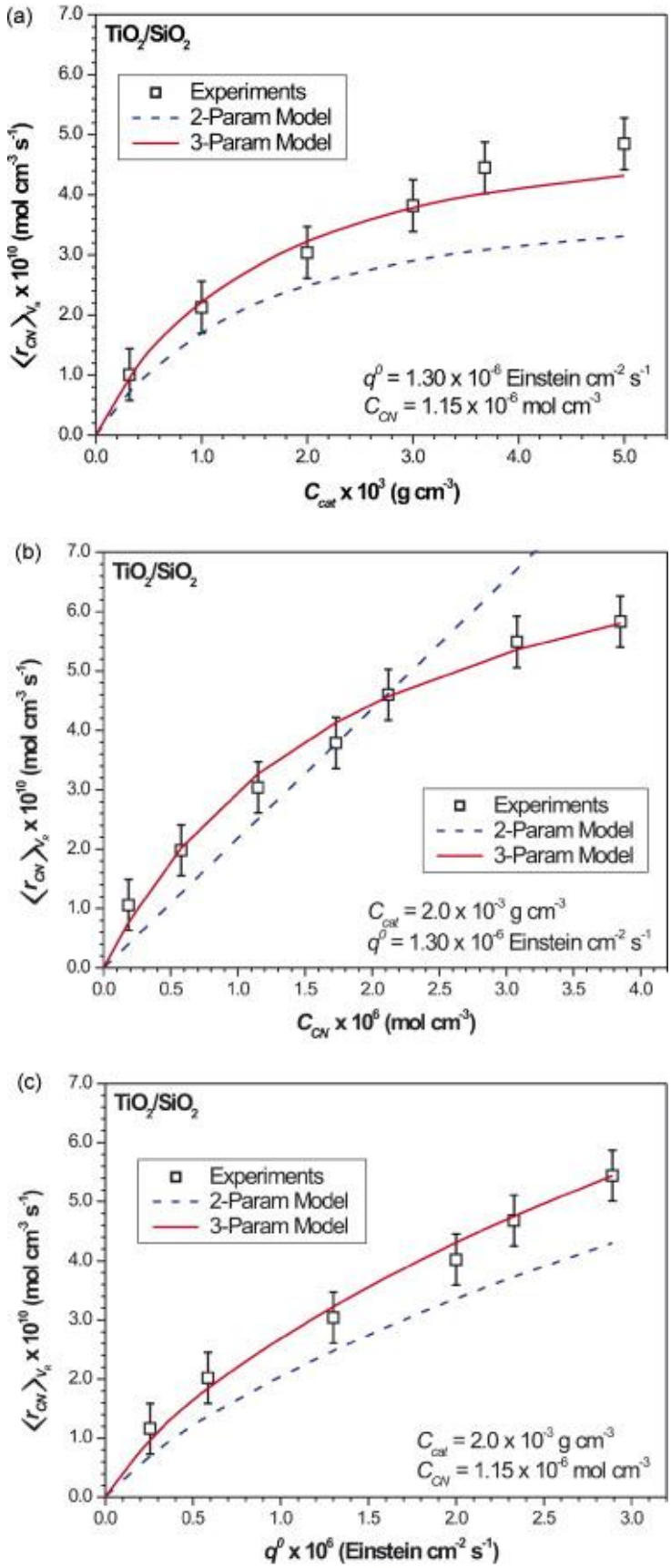

Figure 4. Experimental results of the initial reaction rate for the cyanide photocatalytic oxidation with TiO_2/SiO_2 and two and three-parameter model using eqs. (9) and (11).

Summarizing, within the range of the explored variables and employing experimental data of initial reaction rates, the kinetics of the process that uses pure titanium dioxide can be satisfactorily described by the simplified model represented by Eq. (10) with only two parameters. Differently, when supported titanium dioxide on silica is employed, the model that describes the reaction kinetics must make use of three parameters as shown by Eq. (9). This last result could be an indication that the presence of silica could be introducing a significant modification in the adsorption equilibrium of the cyanide ion.

5. CONCLUSIONS

The kinetic model for the photocatalytic oxidation of cyanide developed in this work as well as its correspondent procedures for the evaluation of the LVRPA distribution inside the photoreactor and the estimation of the kinetic parameters have been successfully validated with both powder TiO_2 and TiO_2 supported on silica. In both cases, the model reproduces the influence on the reaction rate of the catalyst loading, the initial cyanide concentration, and the inlet radiation flux with normalized root mean square errors below 5 %.

The developed model, based on a rigorous reaction mechanism and accounting explicitly for the local volumetric rate of photon absorption, constitutes an intrinsic kinetic description of the photocatalytic oxidation reaction. Therefore, it can be used in a predictive way for the simulation and optimization of any other reactor configuration for the photocatalytic oxidation of cyanide as well as photoreactor design or scaling-up purposes.

ACKNOWLEDGEMENTS

The authors gratefully acknowledge the financial support of the Ministerio de Educación y Ciencia of Spain through the program Consolider-Ingenio 2010 (project CSD2006-00044 TRAGUA) and the international action PCI2006-A7-0526, Comunidad de Madrid through the program REMTAVARES S-0505/AMB/0395 and from the Universidad Nacional del Litoral, Agencia Nacional de Promoción Científica y Tecnológica, and Consejo Nacional de Investigaciones Científicas y Técnicas of Argentina. Thanks are also due to Ing. Irene Alvárez for her help with some of the experiments.

APPENDIX A. Derivation of the kinetic model.

On the basis of the adopted reaction scheme summarized in Table 2, the photocatalytic degradation of cyanide in aqueous solution can be represented as:

$$r_{CN^-}^{S} = -k_9[CN^-][h^+] - k_{10}[CN^-][\equiv TiO\bullet] + k_{13}[(CN)_2][HO^-]^2 \quad (A.1)$$

By applying the kinetic micro steady state approximation (MSSA) for the concentration of electrons, holes, hydroperoxyl radicals ($HO_2\bullet$), superoxide ion radicals ($O_2^-\bullet$), and surface trapped holes ($\equiv TiO\bullet$), we obtain:

$$r_{e^-} = r_g - k_2[e^-][h^+] - k_3[e^-][O_2] - k_5[e^-][HO_2\bullet] - k_{11}[e^-][\equiv TiO\bullet] \approx 0 \quad (A.2)$$

$$r_{h^+} = r_g - k_2[e^-][h^+] - k_6[h^+][\equiv TiO^-] - k_7[h^+][HO^-] - k_9[h^+][CN^-] \approx 0 \quad (A.3)$$

$$r_{HO_2\bullet} = -k_4[O_2^-\bullet][H_2O] - k_5[e^-][HO_2\bullet] \approx 0 \quad (A.4)$$

$$r_{O_2^-\bullet} = k_3[e^-][O_2] - k_4[O_2^-\bullet][H_2O] \approx 0 \quad (A.5)$$

$$r_{\equiv TiO\bullet} = -k_6[h^+][\equiv TiO^-] - k_8[HO^-][\equiv TiO\bullet] - k_{10}[CN^-][\equiv TiO\bullet] - k_{11}[e^-][\equiv TiO\bullet] \approx 0 \quad (A.6)$$

By assuming that the concentration of electrons and holes are approximately equal ($[e^-] \approx [h^+]$) [49] and that cyanide is mainly oxidized by the surface trapped holes ($k_9[h^+][CN^-] \approx 0$) [17], the expression for the hole concentration can be obtained from Eqs. (A.2) to (A.6):

$$[h^+] = \alpha\left(-1 \pm \sqrt{1 + \frac{r_g}{\alpha^2}}\right) \quad (A.7)$$

Here the positive root is the only one that has physical meaning and α is defined as

$$\alpha = \frac{k_6[\equiv TiO^-] + k_7[HO^-]}{2k_2} \quad (A.8)$$

Introducing Eq. (A.7) into Eq. (A.6) and assuming that $k_{11}[e^-] = k_{11}^*$ [17], the expression for the surface trapped holes is obtained:

$$[\equiv \mathrm{TiO}\bullet] = \frac{\alpha k_6[\equiv \mathrm{TiO}^-]}{k_8[\mathrm{HO}^-] + k_{10}[\mathrm{CN}^-] + k_{11}^*}\left(-1 + \sqrt{1 + \frac{r_g}{\alpha^2}}\right) \tag{A.9}$$

The kinetic MSSA can be applied to the radical CN•:

$$r_{CN\bullet} = k_{10}[\mathrm{CN}^-][\equiv \mathrm{TiO}\bullet] - 2k_{12}[\mathrm{CN}\bullet]^2 \approx 0 \tag{A.10}$$

Considering that $(CN)_2$ is an unstable species, we can write:

$$r_{(CN)_2} = k_{12}[\mathrm{CN}\bullet]^2 - k_{13}[(\mathrm{CN})_2][\mathrm{HO}^-]^2 = \tfrac{1}{2}k_{10}[\mathrm{CN}^-][\equiv \mathrm{TiO}\bullet] - k_{13}[(\mathrm{CN})_2][\mathrm{HO}^-]^2 \approx 0 \tag{A.11}$$

From Eqs. (A.11) and Eq. (A.1), we arrive to the following equation

$$r_{CN^-}^S = -\tfrac{1}{2}k_{10}[\mathrm{CN}^-][\equiv \mathrm{TiO}\bullet] \tag{A.12}$$

Introducing Eq. (A.9) into Eq. (A.12) and assuming that (i) the rate of electron-hole generation is proportional to the local volumetric rate of photon absorption (e^a) [27] and (ii) the concentrations of water and hydroxyl ions on the catalytic surface are almost constant, the cyanide photocatalytic degradation rate can be represented as

$$r_{CN^-}^S = -\frac{\alpha_1'[\mathrm{CN}^-]}{1 + \alpha_3'[\mathrm{CN}^-]}\left[-1 + \sqrt{1 + \frac{\alpha_2}{S_g C_{cat}}e^a}\right] \tag{A.13}$$

where

$$\alpha_1' = \frac{k_6 k_{10}[\equiv \mathrm{TiO}^-]}{4k_2}\,\frac{k_6[\equiv \mathrm{TiO}^-] + k_7[\mathrm{HO}^-]}{k_8[\mathrm{HO}^-] + k_{11}^*} \tag{A.14}$$

$$\alpha_2 = \overline{\varphi}\left(\frac{2k_2}{k_6[\equiv \mathrm{TiO^-}] + k_7[\mathrm{HO^-}]}\right)^2 \quad \text{(A.15)}$$

$$\alpha_3^{'} = \frac{k_{10}}{k_8[\mathrm{HO^-}] + k_{11}^{*}} \quad \text{(A.16)}$$

The kinetic model assumes that photocatalytic reactions occur at the catalyst surface among adsorbed species and that dynamic equilibrium is achieved between adsorbed and bulk concentrations of organic compounds. Competitive adsorption of cyanide and the main intermediate products is also postulated. On the contrary, a non-competitive adsorption of oxygen on the catalyst surface sites is considered [49]. Consequently, the following equations can be written:

$$[\mathrm{CN^-}] = K_{CN^-}\,[\mathrm{site}][\mathrm{CN_b^-}] \quad \text{(A.17)}$$

$$[\mathrm{P}] = K_P\,[\mathrm{site}][\mathrm{P}_b] \quad \text{(A.18)}$$

where $[\mathrm{CN_b^-}]$ and $[\mathrm{P}_b]$ are the concentrations of cyanide and intermediate compounds in the suspension bulk, K_{CN^-} and K_P are the equilibrium adsorption constants of cyanide and intermediate products, and $[\mathrm{site}]$ represents the superficial concentration of vacant adsorption sites. By making a balance of sites and employing the Eqs. (A.17) and (A.18), it is possible to obtain:

$$[\mathrm{CN^-}] = \frac{[\mathrm{site_{tot}}]\,K_{CN^-}[\mathrm{CN_b^-}]}{1 + K_{CN^-}[\mathrm{CN_b^-}] + \sum_P K_P[\mathrm{P}_b]} \quad \text{(A.19)}$$

From Eqs. (A.13) and (A.19), the cyanide photocatalytic degradation rate per unit surface area is given by

$$r_{CN^-}^{S} = -\frac{\alpha_1[\mathrm{CN_b^-}]}{1 + \alpha_3[\mathrm{CN_b^-}] + \sum_P K_P[\mathrm{P}_b]}\left[-1 + \sqrt{1 + \frac{\alpha_2}{S_g C_{cat}}e^{a}}\right] \quad \text{(A.20)}$$

where

$$\alpha_1 = \frac{k_6 k_{10}[\equiv \mathrm{TiO}^-]}{4k_2} \frac{k_6[\equiv \mathrm{TiO}^-] + k_7[\mathrm{HO}^-]}{k_8[\mathrm{HO}^-] + k_{11}^*} K_{CN^-}[\mathrm{site_{tot}}] \quad \text{(A.21)}$$

$$\alpha_2 = \overline{\varphi}\left(\frac{2k_2}{k_6[\equiv \mathrm{TiO}^-] + k_7[\mathrm{HO}^-]} \right)^2 \quad \text{(A.22)}$$

$$\alpha_3 = \frac{k_8[\mathrm{HO}^-] + k_{10}[\mathrm{site_{tot}}] + k_{11}^*}{k_8[\mathrm{HO}^-] + k_{11}^*} K_{CN^-} \quad \text{(A.23)}$$

Finally, the cyanide photocatalytic degradation rate per unit suspension volume can be obtained by the product of the cyanide photocatalytic degradation rate per unit surface area ($r_{CN^-}^S$) and the catalyst surface area per unit volume (a_v):

$$r_{CN^-} = r_{CN^-}^S \, a_v = r_{CN^-}^S \, S_g C_{cat} \quad \text{(A.24)}$$

APPENDIX B. Numerical Resolution of the Radiative Transfer Equation (RTE).

This appendix describe the numerical resolution of the Radiative Transfer Equation (RTE) using the Discrete Ordinate Method (DOM). The basic idea behind this method is the transformation of the integro-differential RTE into a system of algebraic equations that describe the transport of photons in such way that they can be solved following the direction of propagation, starting from the values provided by the boundary condition.

As shown in a previous work [48], the low absorption coefficients of the TiO_2/SiO_2 photocatalyst, in comparison with pure TiO_2 suspensions, requires the use of a cylindrical two-dimensional (r,z) − two-directional (θ,ϕ) model of the photoreactor radiation field. Figure B.1 shows the directional and spatial discretization of the cylindrical photoreactor.

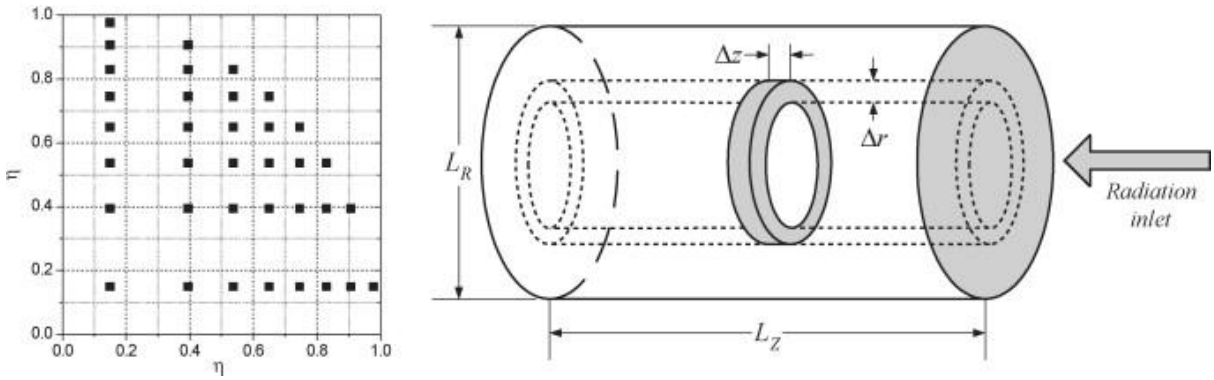

Figure B.1. Gaussian quadrature scheme used for the discretization of the spherical space of directions as a function of the direction cosines (μ,η) (left) and the spatial mesh defined for the 2-D discretization of the cylindrical reactor (right).

For multidimensional geometries, Duderstadt and Martin [61] recommended the derivation of finite difference relations directly from the radiation balance for each mesh cell instead of introducing the finite difference approximation into the RTE. Considering the spatial cell represented in Figure B.2, the spherical space of directions can be divided into four quadrants. The set of directions corresponding to every quadrant is solved by calculating the intensity in the center of the cell from the two surfaces through which the radiation is entering and also calculating the outgoing radiation fluxes through the opposite surfaces. As

it can be observed, the inlet and outlet surfaces depend on the quadrant of the considered direction of propagation.

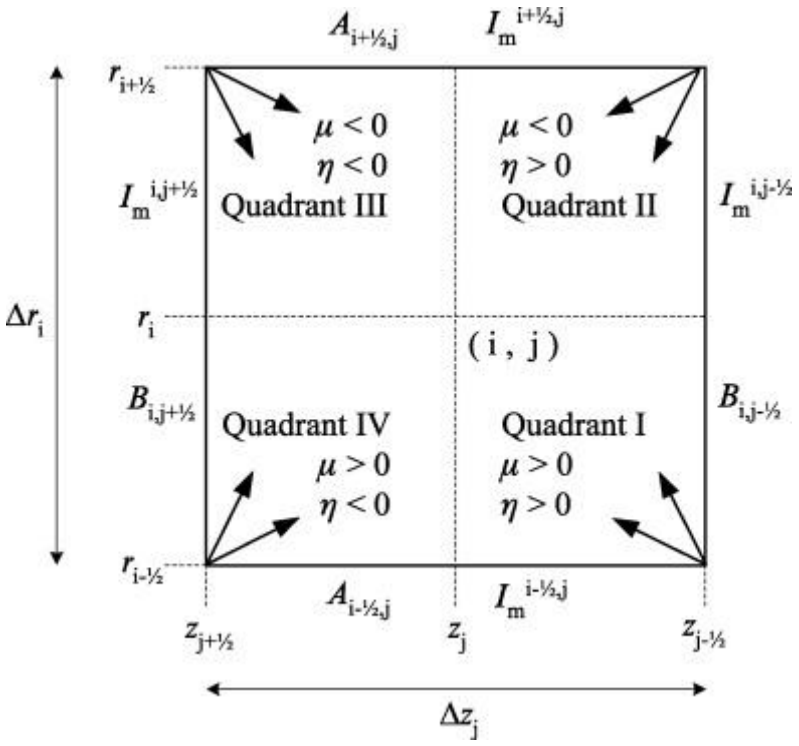

Figure B.2. Definition of the spatial cell and the quadrants of directions as a function of the direction cosines (μ,η) respect to *z* and *r* axis (bottom).

The balance of photons with a given wavelength λ propagated through the cell along the direction $\Omega_m\,(\mu,\eta)$ can be expressed as follows:

$$\underbrace{\mu_m\ A_{i+1/2,j} I_m^{i+1/2,j} - A_{i-1/2,j} I_m^{i-1/2,j} + \eta_m\ B_{i,j+1/2} I_m^{i,j+1/2} - B_{i,j-1/2} I_m^{i,j-1/2}}_{\text{inlet and oulet radiation fluxes}} +$$

$$\underbrace{A_{i+1/2,j} - A_{i-1/2,j}\ \cdot\ \nu_{m+1/2} I_{m+1/2}^{i,j} / w_m - \nu_{m-1/2} I_{m-1/2}^{i,j} / w_m}_{\text{angular redistribution term}} + \qquad \text{(B.1)}$$

$$\underbrace{\kappa_\lambda I_m^{i,j} V_{i,j} + \sigma_\lambda I_m^{i,j} V_{i,j}}_{\text{absorption and out-scattering}} = \underbrace{\frac{\sigma_\lambda}{4\pi} \sum_{n=1}^{M} I_n^{i,j} p_{nm} w_n V_{i,j}}_{\text{in-scattering}}$$

where the areas and volume of the spatial cell are given by:

$$A_{i+1/2,j} = 2\pi r_{i+1/2}\Delta z_j \tag{B.2}$$

$$B_{i,j+1/2} = 2\pi[(r_{i+1/2} + r_{i-1/2})/2]\Delta r_i \tag{B.3}$$

$$V_{i,j} = 2\pi[(r_{i+1/2} + r_{i-1/2})/2]\Delta r_i \Delta z_j \tag{B.4}$$

and $\nu_{m-1/2}$ and $\nu_{m+1/2}$ are effective areas for the angular fluxes corresponding to directions $\Omega_{m-1/2}$ and $\Omega_{m+1/2}$, respectively, and w_m is the weight of the direction Ω_m according to the quadrature scheme. These fluxes are originated in the angular redistribution phenomenon that takes place in curvilinear coordinate systems when changes in the directional coordinate μ are produced. They can be calculated as:

$$\nu_{m+1/2} - \nu_{m-1/2} = -\mu_m w_m \tag{B.5}$$

A detailed explanation of angular redistribution problem can be found in the work of Romero et al. [62].

If the values of Δr and Δz are small enough to consider lineal profiles inside the spatial cell, the central intensity can be expressed as:

$$I_m^{i,j} = (I_m^{i-1/2,j} + I_m^{i+1/2,j})/2 \tag{B.6}$$

$$I_m^{i,j} = (I_m^{i,j-1/2} + I_m^{i,j+1/2})/2 \tag{B.7}$$

and for the directional mesh:

$$I_m^{i,j} = (I_{m-1/2}^{i,j} + I_{m+1/2}^{i,j})/2 \tag{B.8}$$

Substituting in the photon balance [Eq. (B.1)], the central intensity can be calculated according to:

$$I_m^{i,j} = |\mu_m|(A_{i+1/2,j} - A_{i-1/2,j})D^{-1}I_m^{i\pm1/2,j} + 2|\eta_m|B_{i,j}D^{-1}I_m^{i,j\pm1/2} +$$
$$(A_{i+1/2,j} - A_{i-1/2,j})\cdot(\nu_{m+1/2} + \nu_{m-1/2})D^{-1}w_m^{-1}I_{m-1/2}^{i,j} + \qquad \text{(B.9)}$$
$$\frac{\sigma_\lambda}{4\pi}\sum_{n=1}^{M} I_n^{i,j} p_{nm} w_n V_{i,j} D^{-1}$$

where

$$D = |\mu_m|(A_{i+1/2,j} + A_{i-1/2,j}) + 2|\eta_m|B_{i,j} +$$
$$(A_{i+1/2,j} - A_{i-1/2,j})\cdot(\nu_{m+1/2} + \nu_{m-1/2})w_m^{-1} + \kappa_\lambda V_{i,j} + \sigma_\lambda V_{i,j} \qquad \text{(B.10)}$$

Figure B.3 represents the cross section of the spatial mesh of the photoreactor in which the system of algebraic equations constituted by Eqs. (B.6) to (B.9) has to be solved. With this purpose, the symmetry condition is assumed in the axis of the cylinder (that means that at $r = 0$ quadrants I and IV are symmetric with respect to quadrants II and III, respectively) and the following boundary conditions are used:

i) Known inlet radiation for quadrants I and II at $z = 0$.
ii) Null reflection in the inner reactor walls surfaces. Consequently the inlet radiation is null for quadrants II and III $r = L_R$, and quadrants III and IV at $z = L_Z$.

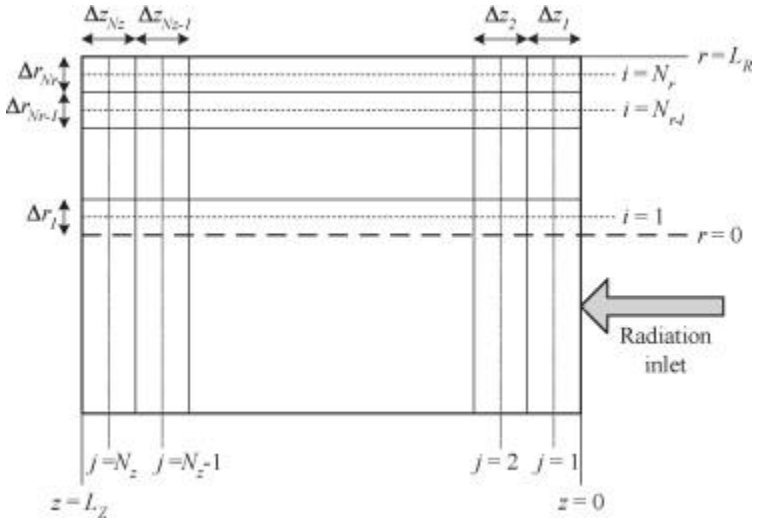

Figure B.3. Cross section of the spatial mesh of the photoreactor.

The algorithm developed to solve the system of equations is schematized in Figure B.4. As it can be seen, the computation of every quadrant begins from the corner of the spatial mesh in which two of the four conditions can be applied. The directional mesh is always calculated from $m = 1$ to $m = M$, being $m = 1$ the direction more parallel to the *r*-*z* plane, in which the angular redistribution could be considered as negligible ($I^{i,j}_{m-1/2} = 0$). First, the central intensity is calculated from the inlet values, and then the outlet intensities are obtained. Convergence of the radiation field is achieved when the intensities initially employed for the calculus of the in-scattering terms coincide with the calculated values.

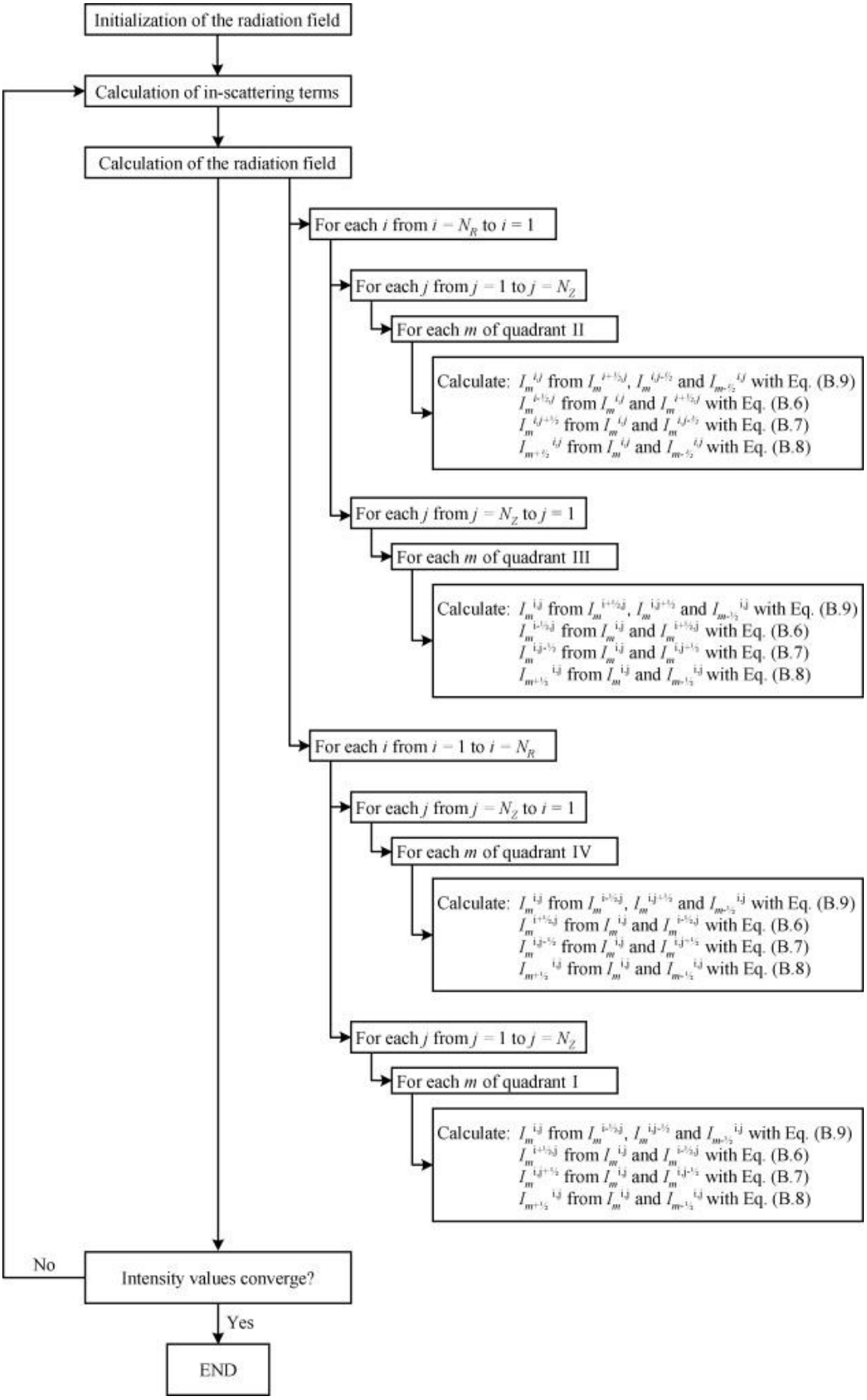

Figure B.4. Algorithm implemented for the resolution of the RTE in curvilinear coordinate systems with angular redistribution using the DOM.

NOMENCLATURE

a_v	catalyst surface area per unit volumen, cm^{-1}
A	area of the spatial cell parallel to the cylindrical axe, cm^2
B	area of the spatial cell perpendicular to the cylindrical axe, cm^2
C_{cat}	catalyst mass concentration, $g\ m^{-3}$
C_{CN^-}	cyanide molar concentration, $mol\ cm^{-3}$
e^a	local volumetric rate of photon absorption, Einstein $cm^{-3}\ s^{-1}$
F	F-value
g	asymmetry factor of the Henyey-Greentein's phase function, dimensionless
I	radiation intensity, Einstein $cm^{-2}\ s^{-1}\ sr^{-1}$
k	kinetic constant, $cm^2\ mol^{-1}\ s^{-1}$
K	equilibrium adsorption constant, $cm^3\ mol^{-1}$
NRMSE	normalized root mean square error, %
p	phase function, dimensionless
P	cyanide degradation intermediate product
q^0	inlet radiation flux, Einstein $cm^{-2}\ s^{-1}$
r	radial cylindrical coordinate, cm
r_{CN^-}	cyanide photooxidation reaction rate, $mol\ cm^{-3}\ s^{-1}$
s	linear coordinate along the direction of radiation propagation $\underline{\Omega}$, cm
S_g	TiO_2 specific surface area of the catalyst, $cm^2\ g^{-1}$
t	time, s
V	volume, cm^3
$\underline{x}$	position vector in a 3D space, cm
w	weight, dimensionless
z	axial cylindrical coordinate, cm

Greek letters

α	angle between the direction of the incident and the scattered rays, rad
α_1	kinetic parameter, $cm\ s^{-1}$
α_2	kinetic parameter, $cm^2\ s\ Einstein^{-1}$
α_3	kinetic parameter, $cm^3\ mol^{-1}$
ε_L	liquid hold-up, dimensionless
ϕ	spherical coordinate, rad

$\bar{\varphi}$ wavelength averaged primary quantum yield, mol Einstein^{-1}

η direction cosine, dimensionless

κ napierian volumetric absorption coefficient, cm^{-1}

λ wavelength, nm

μ direction cosine, dimensionless

ν effective area for angular fluxes, cm^2

θ spherical coordinate, rad

σ napierian volumetric scattering coefficient, cm^{-1}

Ω solid angle of radiation propagation about the direction $\underline{\Omega}$, sr

$\underline{\Omega}$ unit vector in the direction of radiation propagation

Subscripts

b relative to the bulk suspension

CN^- relative to cyanide

P relative to an intermediate degradation product

R relative to the reactor

T relative to the total recirculating system

Tk relative to the reservoir tank

V_R relative to the reactor volume

λ indicates a dependence on wavelength

$\underline{\Omega}$ indicates a directional dependence

Superscripts

0 indicates initial condition

Exp experimental value

KM relative to the kinetic model

s relative to the reaction rate per unit surface area

Special symbols

_ indicates a vectorial magnitude

[] concentration on the catalyst surface, mol cm^{-2}

$\langle\ \rangle$ indicates average value

REFERENCES

[1] P. Kjeldsen, Water Air Soil Poll. 115 (1999) 279-307.

[2] A. Durán, J.M. Monteagudo, I. San Martín, F. Garcia-Peña, P. Coca, J. Hazard Mater. 144 (2007) 132-139.

[3] W.S. Rader, L. Solujic, E.B. Milosavljevic, J.L. Hendrix, Environ. Sci. Technol. 27 (1993) 1875-1879.

[4] R. van Grieken, J. Aguado, M.J. López-Muñoz, J. Marugán, Gold Bull. 38/4 (2005) 180-187.

[5] C.A. Young, T.S. Jordan, Proceedings of the 10th annual conference on hazardous waste research, Kansas State University, Manhattan, Kansas, 1995, pp. 104-129.

[6] S.N. Frank, A.J. Bard, J. Am. Chem. Soc. 99 (1977) 303-304.

[7] D.F. Ollis, H. Al-Ekabi (Eds.), Photocatalytic purification and treatment of water and air, Elsevier, Amsterdam, 1993.

[8] D. Blake, Bibliography of work on the photocatalytic removal of hazardous compounds from water and air, NREL, Golden, CO; May 1994. (1st update: October 1994; 2nd update: October 1996; 3rd update: January 1999; 4th update: October 2001).

[9] M.R. Hoffmann, S.T. Martin, W. Choi, D.W. Bahnemann, Chem. Rev. 95 (1995) 69-96.

[10] J.M. Herrmann, Catal. Today 53 (1999) 115-129.

[11] D.S. Bhatkhande, V.G. Pangarkar, A.A. Beenackers, J. Chem. Technol. Biotechnol. 77 (2001) 102-116.

[12] A. Mills, S.K. Lee, Semiconductor photocatalysis, in Advanced oxidation processes for water and wastewater treatment, S. Parsons (Ed.), IWA Publishing, London, UK, 2004.

[13] A.G. Agrios, P. Pichat, J. Appl. Electrochem. 35 (2005) 655-663.

[14] T.L. Rose, C. Nanjundiah, J. Phys. Chem. 89 (1985) 3766-3771.

[15] J. Peral, J. Muñoz, X. Domènech, J. Photochem. Photobiol. A:Chem. 55 (1990) 251-257.

[16] V. Augugliaro, V. Loddo, G. Marcì, L. Palmisano, M.J. López, J. Catal., 166 (1997) 272-283.

[17] K. Chiang, R. Amal, T. Tran, J. Molec. Catal. A:Chem. 193 (2003) 285-297.

[18] V. Augugliaro, E. García López, V. Loddo, M.J. López-Muñoz, G. Marcì, L. Palmisano, M. Schiavello, Fresenius Environ. Bull. 8 (1999) 350-357.

[19] R. van Grieken, J. Aguado, M.J. López-Muñoz, J., Marugán, Appl. Catal B:Environ. 55 (2005) 201-211.

[20] V. Augugliaro, J.C. Conesa, E. García López, V. Loddo, M.J. López Muñoz, G. Marcì, L. Palmisano, M. Schiavello, J. Soria, Chimica e L'industria 83 (2001) 34.

[21] A. Vidal, P. Trincado, M. Jerez, M. Vincent, J. Blanco, S. Malato, P. Fernández, Ingeniería Química, Enero (2001) 161-165.

[22] C. Minero, Solar Energy Mater. Solar Cells 38 (1995) 421-430.

[23] A. Mills, J. Wang, D.F. Ollis, J. Catal. 243 (2006) 1-6.

[24] S. Brosillon, L. Lhomme, C. Vallet, A. Bouzaza, D. Wolbert, Appl. Catal. B: Environ. 78 (2008) 232-241.

[25] L. Vincze, T.J. Kemp., J. Photochem. Photobiol. A:Chem. 87 (1995) 257-260.

[26] L. Rideh, A. Wehrer, D. Ronze, A. Zoulalian, Ind. Eng. Chem. Res. 36 (1997) 4712-4718.

[27] O.M. Alfano, M.I. Cabrera, A.E. Cassano, J. Catal. 172 (1997) 370-379.

[28] C.S. Zalazar, R.L. Romero, C.A. Martín, A.E. Cassano, Chem. Eng. Sci. 60 (2005) 5240-5254.

[29] B. Bayarri, J. Giménez, D. Curcó, S. Esplugas, Catal. Today, 101 (2005) 227-236.

[30] M. Rodríguez, S. Malato, C. Pulgarin, S. Contreras, D. Curcó, J. Giménez, S. Esplugas, Solar Energy 79 (2005) 360-368.

[31] B. Toepfer, A. Gora, G. Li Puma, Appl. Catal. B:Environ. 68 (2006) 171-180.

[32] I. Salvado-Estivill, D.M Hargreaves, G. Li Puma, Environ. Sci. Technol. 41 (2007) 2028-35.

[33] G. Camera-Roda, F. Santarelli, F. Catal. Today 129 (2007) 161-168.

[34] M.C. Hidalgo, M Aguilar, M. Maicu, J.A. Navío, G. Colón, Catal. Today 129 (2007) 50-58.

[35] E. Bermudez, J.B. Mangum, B.A. Wong, B. Asgharian, P.M. Hext, D.B. Warheit, J.I. Everitt, Toxicol. Sci. 77 (2004) 347-357.

[36] J.R. Gurr, A.S.S. Wang, C.H. Chen, K.Y. Jan, Toxicol. 213 (2005) 66-73.

[37] R.L. Pozzo, M.A. Baltanás, A.E. Cassano, Catal. Today 39 (1997) 219-231.

[38] A. Alexiadis, I. Mazzarino, Chem. Eng. Process. 44 (2004) 453-459.

[39] M.G. Chiovetta, R.L. Romero, A.E. Cassano, Chem. Eng. Sci. 56 (2001) 1631-1638.

[40] T. Kanki, S. Hamasaki, S. Shinpei, T. Noriaki, A. Toyoda, K. Hirano, Chem. Eng. J. 108 (2005) 155-160.

[41] B.S. Lee, D.J. Kang, S.G. Kim, J. Mater. Sci. 38 (2003) 3545-3552.

[42] J. Aguado, R. van Grieken, M.J. López-Muñoz, J. Marugán, Appl. Catal. A:Gen. 312 (2006) 202-212.

[43] J. Aguado, R. van Grieken, M.J. López-Muñoz, J. Marugán, Catal. Today 75 (2002) 95-102.

[44] J. Marugán, M.J. López-Muñoz, J. Aguado, R. van Grieken, Catal. Today 124 (2007) 103-109.

[45] J. Marugán, R. van Grieken, O.M. Alfano, A.E. Cassano, AIChE J. 52 (2006) 2832-2843.

[46] J. Marugán, R. van Grieken, O.M. Alfano, A.E. Cassano, Int. J. Chem. Reactor Eng. 5 (2007) A89.

[47] L.S. Clescerl, A.E. Greenberg, A.D. Eaton (Eds.), Standard methods for the examination of water and wastewater, United Book Press Inc., Baltimore, 1998.

[48] J. Marugán, R. van Grieken, A.E. Cassano, O.M. Alfano, Catal. Today 129 (2007) 143-151.

[49] C.S. Turchi, D.F. Ollis, J. Catal. 122 (1990) 178-192.

[50] M.N. Ozisik, Radiative transfer and interactions with conduction and convection, Wiley, New York, 1973.

[51] M.L. Satuf, R.J. Brandi, A.E. Cassano, O.M. Alfano, Ind. Eng. Chem. Res., 44 (2005) 6643-6649.

[52] M. Pasquali, F. Santarelli, J.F. Porter, P.L. Yue, AIChE J. 42 (1996) 532-537.

[53] T. Yokota, S. Cesur, H. Suzuki, H. Baba, Y. Takahata, J. Chem. Eng. Jpn. 32 (1999) 314-321.

[54] D. Curcó, J. Giménez, A. Addardak, S. Cervera-March, S. Esplugas, Catal. Today 76 (2002) 177-188.

[55] Q. Yang, P.L. Ang, M.B. Ray, S.O. Pehkonen, Chem. Eng. Sci. 60 (2005) 5255-5268.

[56] M.I. Cabrera, O.M. Alfano, A.E. Cassano, J. Adv. Oxid. Technol. 3 (1998) 220-228.

[57] G. Slagari, G. Camera-Roda, F. Santarelli, Int. Commun. Heat Mass Transfer 5 (1998) 651-660.

[58] C.A. Arancibia-Bulnes, J.C. Ruiz-Suarez, Appl. Optics 38 (1999) 1877-1883.

[59] A.E. Cassano, O.M. Alfano, Catal. Today 58 (2000) 167-197.

[60] R.J. Brandi, M.A. Citroni, O.M. Alfano, A.E. Cassano, Chem. Eng. Sci. 58 (2003) 979-985.

[61] J.J. Duderstadt, W.R. Martin, Transport theory, Wiley, New York, 1979.

[62] R.L. Romero, O.M. Alfano, A.E. Cassano, Ind. Eng. Chem. Res. 36 (1997) 3094-3109.